Inorganic Chemistry
Cite This: Inorg. Chem. 2019, 58, 1241−1251
Article
pubs.acs.org/IC

# Pyrochlore Rare-Earth Hafnate $RE_2Hf_2O_7$ (RE = La and Pr) Nanoparticles Stabilized by Molten-Salt Synthesis at Low Temperature

Madhab Pokhrel,[†,‡] Santosh K. Gupta,[†,§] Kareem Wahid,[†,‡] and Yuanbing Mao*[,†,∥]

[†]Department of Chemistry, University of Texas Rio Grande Valley, 1201 West University Drive, Edinburg, Texas 78539, United States

[‡]Department of Physics, University of Texas Rio Grande Valley, 1201 West University Drive, Edinburg, Texas 78539, United States

[§]Radiochemistry Division, Bhabha Atomic Research Centre, Trombay, Mumbai-400085, India

[∥]School of Earth, Environmental, and Marine Sciences, University of Texas Rio Grande Valley, 1201 West University Drive, Edinburg, Texas 78539, United States

Supporting Information

**ABSTRACT:** Complex oxides of the $RE_2Hf_2O_7$ series are functional materials that exist in the fluorite or pyrochlore phase depending on synthesis method and calcination temperature. In this study, we investigate the process of synthesis, crystal structure stabilization, and phase transition in a series of RE hafnate compounds, synthesized by the coprecipitation process of a single-source complex hydroxide precursor followed with direct calcination or molten-salt synthesis (MSS) method. Phase pure $RE_2Hf_2O_7$ (RE = Y, La, Pr, Gd, Er, and Lu) ultrafine nanostructured powders were obtained after calcinating the precursor in a molten salt at 650 °C for 6 h. Moreover, we demonstrate that the MSS method can successfully stabilize ideal pyrochlore structures for $La_2Hf_2O_7$ and $Pr_2Hf_2O_7$ in the nanodomain, which is not possible to achieve by direct calcination of the coprecipitated precursor at 650 °C. We propose mechanisms to elucidate the differences in these two synthesis methods and highlight the superiority of the MSS method for the production of RE hafnate nanoparticles.

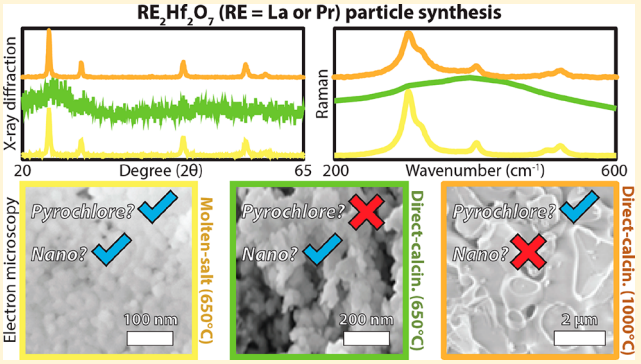


## 1. INTRODUCTION

The search for synthesis methods which are simple, green, reliable, scalable, and generalizable for stable pyrochlores such as rare earth hafnates $RE_2Hf_2O_7$ (REHfO) has been an area of interest for many researchers in recent years.[1−5] $RE_2Hf_2O_7$ (RE = La, Pr) adopting the pyrochlore (space group $Fd\bar{3}m$) structure, closely related to the disordered fluorite structure ($Fm\bar{3}m$), falls in the class of complex oxide materials. The stability of pyrochlore and fluorite structures is generally governed by the relative radius of A and B cations. Each of these structures has their own important characteristics. Fluorite based systems such as $Gd_2Zr_2O_7$ and $^{241}Am_2Zr_2O_7$ are much more suitable for nuclear waste hosts when compared to pyrochlores as they have greater radiation stability due to their ability to dissipate excess radiation energy by forming antisite defects.[4,6] In addition, since fluorites have a greater concentration of oxygen-related defects, they can be more productive for use in ionic conductors.[7] Conversely, ideal pyrochlores are much more suitable as heat-resistant oxide ceramics and protective antioxidant coatings.[8]

These hafnates are important not only from a technical perspective but also because they have found applications in many areas of scientific importance. In particular, $Y_2Hf_2O_7$ (YHfO) is proposed to be used in high-energy nuclear medical fields such as computed tomography (CT) and positron emission tomography (PET).[9] $La_2Hf_2O_7$ (LaHfO) is envisaged to be a very good dielectric material due to its small number of defect densities and lower Fermi level pinning than $HfO_2$ itself.[10,11] Additionally, because of its high stopping power for X- and $\gamma$-rays with $Z_{Hf}$ = 72 and high density of 7.9 g/cm$^3$, it is attractive for use in novel high-energy radiation detectors.[11] Like LaHfO, $Lu_2Hf_2O_7$ (LuHfO) was also found to be a promising scintillation host material due to its high density (9.95 g/cm$^3$), high atomic number of Lu ($Z$ = 71), and high effective atomic number ($Z_{eff}$ = 68.9) among $RE_2Hf_2O_7$ compositions.[10] Moreover, $Gd_2Hf_2O_7$ (GdHfO) and $Pr_2Hf_2O_7$ (PrHfO) exhibit interesting magnetic properties with spin-ice characteristics.[12,13]

Because both A- and B-site precursors, namely rare earth oxides and $HfO_2$, are refractory in nature, synthesizing rare earth hafnates by the traditional solid-state route requires long

Received: September 24, 2018
Published: January 7, 2019






DOI: 10.1021/acs.inorgchem.8b02728
Inorg. Chem. 2019, 58, 1241−1251

calcination time and temperature greater than 1500 °C.[14] Such demanding synthesis conditions cause obtained particles to suffer from inhomogeneous and coarse sample formation and poor sintering behavior with nonuniform size distribution. These large sized and nonuniform particles are also more prone to poor adhesion to the substrate and loss of coating.[15] For these reasons, the final material may not attain the desired physical and chemical properties.

Furthermore, high surface area mixed metal oxide nanoparticles (NPs) exhibit superior physical and chemical properties compared to their bulk counterparts. There has been much effort on increasing surface area and decreasing grain size to the nanodomain in order to enhance sinterability and other optical, catalytic, and magnetic properties.[16,17] Along this line, the controlled morphology of NPs also influences the physical and chemical properties of materials and ultimately plays a major role in their applications.[17]

To avoid problems associated with the common solid-state synthesis method, several wet-chemistry based synthetic routes have been reported for the preparation of this type of ternary oxide nanomaterials. Wet-chemistry methods involve mixing precursors at the molecular level, thus producing materials with high compositional homogeneity and stoichiometric control. Common synthetic approaches reported for the preparation of pyrochlore RE hafnates include sol−gel,[18] coprecipitation,[19] hydrothermal,[20,21] gel-combustion,[22,23] complex polymerization,[24] solvothermal,[25] and mechanochemical[26] methods. Unfortunately, these approaches have several drawbacks such as high processing temperature (≥1000 °C) or long exposure time, use of costly raw materials and complex steps, and low crystallinity of the final products.[27] Specifically, the sol−gel method requires long holding times (several 10-h windows) during calcination while the produced particles are hard-agglomerates with nonuniform size. Hydrothermal and solvothermal syntheses require autoclaves for the crystallization of powders while surfactants are necessary to control the size of the formed particles.[17,25] Combustion synthesis has safety-related issues such as the release of $NO_x$ and CO gases, and scaling up for large volume fabrication presents difficulties. Moreover, for non-oxide materials, combustion synthesis should not be a preferred route.

The coprecipitation route is a simple and efficient method to bring composition ions together in single-source complex precursors followed with a calcination step for advanced materials synthesis of complex metal oxides and their nanostructured counterparts. Through this route, many authors have reported low crystallization temperatures, high homogeneity, and high reactivity from evenly coprecipitated precursors, which allows for low processing temperatures.[26,28] However, in the case of complex metal oxides with multiple cations, the precipitation rate varies for different cations, resulting in a mixture of different metal hydroxides as the coprecipitated precursor of a base is used as the precipitant.[29] Furthermore, not all metal ions precipitate completely at the same pH, thus reducing the level of stoichiometric control if the final pH is not high enough.[29] In 2009, we developed a combined coprecipitation and molten salt synthesis procedure to make luminescent nanocrystals with $RE_2B_2O_7$ composition where RE represents rare-earth elements La and Er or their mixtures with oxidation state of +3 and B denotes fourth group transition metallic elements (Hf and Zr) or their mixtures with oxidation state of +4.[30] We realized the importance of generating a single-source complex precursor $RE(OH)_3{\cdot}BO(OH)_2{\cdot}nH_2O$ that contains homogeneously distributed constituting elements, i.e., RE and B at an atomic level. In a typical coprecipitation process, dilute ammonium hydroxide solution is added dropwise to the precursor solutions containing $A^{3+}$ and $B^{4+}$ ions.[5,11,31] However, the role played by the added molten salt during the conversion of this single-source complex precursor into the final $RE_2B_2O_7$ nanocrystals was not known.

Therefore, this study aims to investigate the molten-salt synthesis (MSS) mechanism through comparison with direct calcination (DC) of the coprecipitated single-source complex precursor into $RE_2Hf_2O_7$ (RE = Y, La, Pr, Gd, Er, and Lu) products. We demonstrated how the MSS method can overcome the disadvantages mentioned above and be used to synthesize pure pyrochlore-type LaHfO and PrHfO oxide NPs.

## 2. EXPERIMENTAL SECTION

**2.1. Chemicals.** The starting materials including RE nitrate hydrate ($RE(NO_3)_3{\cdot}xH_2O$, 99.0% (RE = Y, La, Pr, Gd, Er, and Lu), hafnium oxychloride ($HfOCl_2{\cdot}xH_2O$, 99.9%), potassium nitrate ($KNO_3$, 99.9%), sodium nitrate ($NaNO_3$, 98%), and ammonium hydroxide ($NH_4OH$, 28.0−30.0%) were purchased from Sigma-Aldrich. All chemicals are analytical grade reagents and used directly without further purification.

**2.2. Coprecipitation To Form Single-Source Complex Precursor.** In this study, similar to our previous reports,[11,32,33] RE nitrate (RE = Y, La, Pr, Gd, Er, and Lu) and hafnium oxychloride were first dissolved in deionized water. After stirring for 30 min, diluted ammonium hydroxide solution (10%) was added dropwise to the solution under stirring. The rate of dropping was about 50 drops $min^{-1}$. Gel-like precipitates were obtained and subsequently centrifuged/washed with deionized water three times. The washed precipitates were dried at 110 °C in a drying oven overnight and ground to obtain the single-source complex $RE(OH)_3{\cdot}HfO(OH)_2{\cdot}nH_2O$ precursors.

**2.3. DC Processing of the Single-Source Complex Precursor.** The obtained single-source complex $RE(OH)_3{\cdot}HfO(OH)_2{\cdot}nH_2O$ precursors were directly calcinated in air for 6 h at three temperatures, i.e. 650 °C, 1000 °C, and 1500 °C, with a ramp rate of 10 °C/min in a box furnace to obtain $RE_2Hf_2O_7$ powders. The resulting product was washed with copious amounts of deionized water and dried in an oven at 120 °C overnight to obtain the $RE_2Hf_2O_7$ particles.

**2.4. MSS Processing of the Single-Source Complex Precursor.** As another similar but distinct method, 350 mg of the obtained single-source complex precursor $RE(OH)_3{\cdot}HfO(OH)_2{\cdot}nH_2O$ was first ground together with 60 mmol of the nitrate mixture ($NaNO_3$: $KNO_3$ = 1:1, molar ratio) using a ball-mill. The mixture was then transferred into a ceramic crucible, covered, and heated at 650 °C in a box furnace in the air for 6 h with a ramp rate of 10 °C/min. After being cooled to room temperature, the resulting product was washed with copious amounts of deionized water and centrifuged to remove the nitrate salt residual. After being dried in an oven at 120 °C overnight, $RE_2Hf_2O_7$ NPs were obtained.

The overall synthetic procedures are summarized schematically in Figure 1.

**2.5. Characterization.** Powder X-ray diffraction (XRD) patterns of the REHfO powders (RE = Y, La, Pr, Gd, Er, and Lu) were taken with a Bruker D8 ADVANCE, X-ray diffractometer with Cu $K\alpha_1$ radiation ($\lambda$ = 0.15406 nm). The XRD data were collected by utilizing a scanning mode of $2\theta$ ranging from 20° to 70° with a scanning step size of 0.04° and a scanning rate of 1.0° $min^{-1}$. Raman spectra were collected using a Bruker Senterra-system using a 785 nm helium−neon laser with a spatial resolution of 2 $\mu$m, and peaks were fitted with an area version of the Gaussian function using a multiple peak fit tool available in Origin Pro. The morphology of the powders was observed by a field emission scanning electron microscope (Carl Zeiss Sigma VP FESEM) equipped with a field emission gun operated at 5 kV.


DOI: 10.1021/acs.inorgchem.8b02728
Inorg. Chem. 2019, 58, 1241−1251

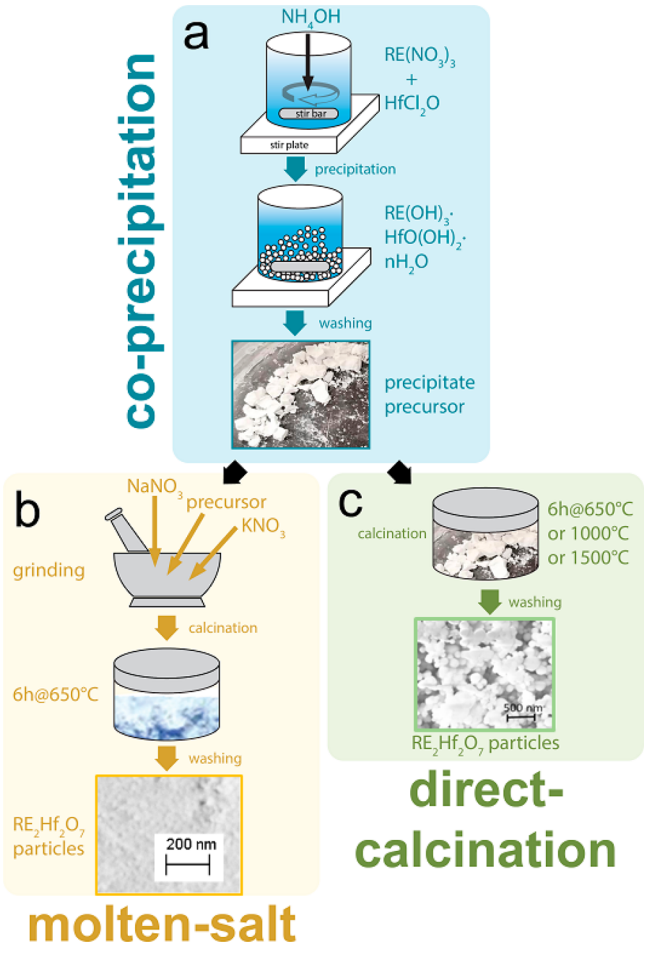


**Figure 1.** Schematic showing (a) coprecipitation, (b) molten-salt synthesis, and (c) direct calcination for the synthesis of the $RE_2Hf_2O_7$ (RE = Y, La, Pr, Gd, Er, and Lu) samples.

## 3. RESULTS AND DISCUSSION

**3.1. Coprecipitation of Complex Precursors.** There is a progressive reduction in ionic radius across the lanthanides series known as lanthanide contraction. This phenomenon is attributed to poor screening of nuclear charge (nuclear attractive force on electrons) by 4f electrons. As a result, the outermost lying 6s electrons are strongly attracted toward the nucleus, thus resulting in a smaller ionic radius with increasing atomic number of lanthanides. This has a profound effect on the physical and chemical properties of lanthanide compounds such as size, shape, and structure, which also changes gradually moving across the series. It was reported that the crystal structure and morphology of rare earth hydroxides, fluorides, and phosphates change gradually with decreasing radii of lanthanide ions.[34−36]

pH has a major role in deciding the precipitation thermodynamics and kinetics. There exist a complex interaction and balance between the chemical potential and the rate of ionic motion. A high pH value indicates higher $OH^-$ ion concentration and a higher chemical potential in solution. Higher $OH^-$ ion concentrations or higher pH may greatly reduce the concentration of the $RE^{3+}$ ion in solution, which is restricted by the value of the solubility product for $RE(OH)_3$ and thus reduces the rate of ionic motion. Greater solubility is shown for larger ionic radii and for lower temperature.[37]

$$RE(OH)_3 \leftrightarrow RE^{3+} + 3OH^-, \quad K_{sp} = [RE^{3+}][OH^-]^3$$

It is also reported that highly charged $Hf^{4+}$ ions hydrolyze easily and tend to polymerize at higher pH because of their higher ionic potential.[38] Using $NH_4OH(aq)$ as the precipitant, as shown in Figure 2a, stable hafnate oxyhydroxide precipitate was formed at pH = 5.0. $RE^{3+}$ ions (Y, Gd, Er, and Lu) precipitate at about pH = 5.0 or below, while $La(NO_3)_3$ and $Pr(NO_3)_3$ begin to form stable precipitates at pH = 8.38 and 7.50, respectively. As far as the formation of hydroxide is

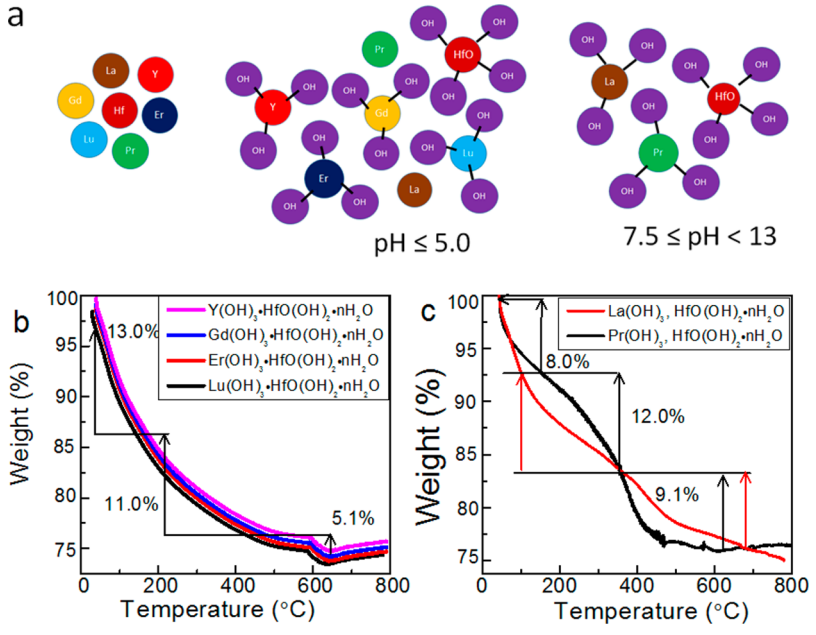


**Figure 2.** (a) Precipitate schematics based on the pH observation as hafnate and $RE^{3+}$ ions (Y, Gd, Er, and Lu) were found to precipitate at pH = 5.0 or below, while $La(NO_3)_3$ and $Pr(NO_3)_3$ begin to precipitate at pH 7.5 or higher. TGA profiles of the single-source complex precursors $RE(OH)_3{\cdot}HfO(OH)_2{\cdot}nH_2O$: (b) RE = Y, Gd, Er, and Lu, and (c) RE = La and Pr.



DOI: 10.1021/acs.inorgchem.8b02728
Inorg. Chem. 2019, 58, 1241−1251

concerned, larger sized lanthanide ions such as La, Ce, Pr, and Nd are preferred to form $RE(OH)_3$ having hexagonal structure whereas medium-sized lanthanide ions from Sm to Tm tend to form $RE_8(OH)_{20}(NO_3)_4{\cdot}nH_2O$.[39] In this study, for simplicity, we use a generic formula $RE(OH)_3{\cdot}HfO(OH)_2{\cdot}nH_2O$ to represent the single-source complex precursor coprecipitated by $NH_4OH$(aq).

Figures S1 and S2 represent the TGA thermogram results for the starting chemicals of $HfOCl_2{\cdot}8H_2O$, $La(NO_3)_3{\cdot}xH_2O$, and $Pr(NO_3)_3{\cdot}xH_2O$, respectively. Figure 2b and 2c show the TGA thermogram results of the formed $RE(OH)_3{\cdot}HfO(OH)_2{\cdot}nH_2O$ (RE = Y, Gd, Er, Lu, La, and Pr) precursor. The thermograms of Y, Gd, Er, and Lu-based precursors appear similar to each other but entirely different from those of La and Pr-based precursors. Figure 2b demonstrates no sharp transition (monotonic behavior) throughout the temperature range below 570 °C indicating water loss is minimal and is equal to about 13.0%. The second interval, between 210 to 420 °C is attributed to the second phase of the reaction as $RE(OH)_3{\cdot}HfO(OH)_2{\cdot}nH_2O \rightarrow REOOH{\cdot}HfOOH + H_2O$. The last interval, between 570 °C and 600 °C can be attributed to the reaction $2REOOH{\cdot}HfOOH \rightarrow RE_2Hf_2O_7 + H_2O$ and corresponds to the complete dehydration and formation of $RE_2Hf_2O_7$ (RE = Y, Gd, Er, and Lu) oxides. The proposed reaction mechanism and the results mentioned above are well in agreement with the previous studies on Gd compounds.[40] The monotonic behavior further indicates that these single-source complex precursors of $RE(OH)_3{\cdot}HfO(OH)_2{\cdot}nH_2O$ (RE = Y, Gd, Er, and Lu) have similar surface area, phase, and morphology. On the other hand, a sharp transition was observed for the La and Pr precursors as shown in Figure 2c. This indicates that the total mass loss (29.1%) over the operating temperature is similar for all Y, Gd, Er, Lu, Pr, and La-based single-source precursors while La and Pr-based single-source precursors display mass loss characteristics at different temperature ranges. In general, rare earth hydroxide dehydration (loss of water molecule) takes place up to 230 °C whereas anionic combustion takes place in two steps at 230−290 °C and 290−600 °C.[39] After 600 °C, all samples reach a plateau indicating no physical or chemical process takes place after this temperature. Interestingly, the thermal behaviors of $RE(OH)_3{\cdot}HfO(OH)_2{\cdot}nH_2O$ (RE = Y, Gd, Er, Lu, La, and Pr) shown in Figure 2b and 2c are in good agreement with the above-mentioned facts regarding rare earth hydroxides. Moreover, the dehydration process is more obvious and sharper from the La and Pr-based single-source complex precursors when compared to the Y, Gd, Er, and Lu-based counterparts. This may be due to higher water retaining capacity (13%) in the Y, Gd, Er, and Lu-based precursors compared to those of La and Pr-based ones (8%), thereby suggesting an increase in the tendency to incorporate $H_2O$ molecules with increasing atomic number (Z) moving across the lanthanide ion series. This phenomenon is related to the strength of H-bonding from nitrate ions of rare earth nitrates; that is, stronger hydrogen bonds lead to greater hydration.[41,42] Therefore, the Y, Gd, Er, and Lu-based precursors have a higher affinity for water compared to the La and Pr-based precursors.

When pH < 7.5, $Y^{3+}$, $Gd^{3+}$, $Er^{3+}$, $Lu^{3+}$, and $Hf^{4+}$ ions have a stronger propensity to form hydroxide by combining with $OH^-$ when compared to $La^{3+}$ and $Pr^{3+}$ ions. Therefore, on the addition of the precipitant $NH_4OH$(aq), hafnium oxyhydroxide and hydroxides of $Y^{3+}$, $Gd^{3+}$, $Er^{3+}$, and $Lu^{3+}$ can precipitate as a single-source complex precursor as $RE(OH)_3{\cdot}HfO(OH)_2{\cdot}nH_2O$, as confirmed by our TGA measurements. When the pH attains a value of 7.5 or higher, the majority of $Hf^{4+}$ ions have already been precipitated out as $HfO(OH)_2$, but $La^{3+}$ and $Pr^{3+}$ ions just start to combine with $OH^-$ to form $La^{3+}$ and $Pr^{3+}$ hydroxides. Thus, the coprecipitates obtained from $La^{3+}$ and $Pr^{3+}$-based solutions are more likely to be a heterogeneous mixture of $Hf^{4+}$and $La^{3+}$ hydroxides and that of $Hf^{4+}$ and $Pr^{3+}$ hydroxides, respectively, rather than a single complex hydroxide precursor of $RE(OH)_3{\cdot}HfO(OH)_2{\cdot}nH_2O$ where RE = Y, Gd, Er, and Lu.

This phenomenon could also be explained in terms of H-bonding formation with nitrates of rare earth ions. Ionic radii of $La^{3+}$ and $Pr^{3+}$ are much larger than $Y^{3+}$, $Gd^{3+}$, $Er^{3+}$, and $Lu^{3+}$ (Table 1)[43] as a consequence of lanthanide contraction.

**Table 1. Ionic Radius of Various 8-Coorinated $RE^{3+}$ Ions[45]**

| $RE^{3+}$ ion in 8-coordination | Ionic Radius (pm) | pH value immediately after initial coprecipitation seen | Final pH value of the coprecepitation solution after adding all $NH_4OH$(aq) solution |
|---|---|---|---|
| La | 116 | 8.38 | 12.2 |
| Pr | 112.6 | 7.5 | 12.2 |
| Y | 101.9 | 4.5 | 12.2 |
| Gd | 105.3 | 5.0 | 12.2 |
| Er | 100.4 | 5.0 | 12.2 |
| Lu | 97.7 | 4.5 | 12.2 |

According to Fajans' rules, smaller $Ln^{3+}$ ions are more polarizing and their salts are correspondingly less ionic which implies that their ionic potential (charge to radius ratio) is relatively lower.[44] Therefore, Y, Gd, Er, and Lu ions form stronger H-bonds and can hold water more efficiently when compared to La and Pr ions. Consequently, $La^{3+}$ and $Pr^{3+}$ ions do not hydrolyze in an acidic medium with pH < 6. In this study, the aqueous solution was kept between pH = 1.86 to 12.2 with the addition of 10% dilute ammonium hydroxide solution using the natural dripping method.

**3.2. X-ray Diffraction Analysis.** The room temperature structure of the $A_2B_2O_7$ composition is dictated by the ionic radius ratio ($r_A/r_B$).[46] It is reported that if $r_A/r_B$ < 1.46, the disordered fluorite phase (DFP) is more likely to form, and if $r_A/r_B$ > 1.46 the ordered pyrochlore phase (OPP) is more likely to be stabilized.

Usually, the DFP to OPP transformation takes place when $r_A/r_B \sim 1.46$. Based on recent studies, it was predicted that $r_A/r_B$ for different $A_2B_2O_7$ compositions obeys the following pattern: DFP $r_A/r_B$ < 1.21 < $\delta$-phase $r_A/r_B$ < 1.42−1.44 < OPP $r_A/r_B$ < 1.78−1.83 < monoclinic pyrochlore $r_A/r_B$ < 1.92.[5] Table 2 depicts the radius ratio for 8-coordinated $A^{3+}$ and 6-

**Table 2. Ionic Radius Ratios and Expected Crystal Structures of Various REHfO Compounds with 8-Coordinated $A^{3+}$ and 6-Coordinated $B^{4+}$ Ions[5,45]**

| $A_2B_2O_7$ composition | $r_A/r_B$ | Expected phase based on radius ratio |
|---|---|---|
| YHfO | 1.26 | DFP |
| LaHfO | 1.45 | OPP |
| PrHfO | 1.39 | OPP |
| GdHfO | 1.32 | Borderline |
| ErHfO | 1.25 | DFP |
| LuHfO | 1.21 | DFP |



DOI: 10.1021/acs.inorgchem.8b02728
Inorg. Chem. 2019, 58, 1241−1251

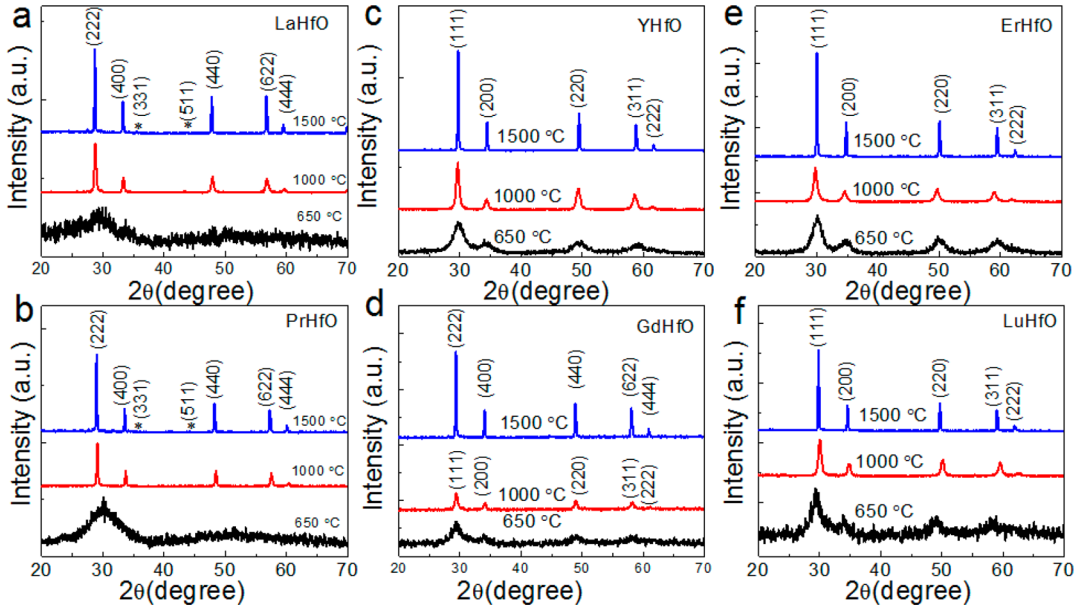


**Figure 3.** XRD patterns of the $RE_2Hf_2O_7$ samples prepared by direct calcination of the single-source complex precursors at 650 °C, 1000 °C, and 1500 °C in air for 6 h.

coordinated $B^{4+}$ ions for various rare earth hafnate compositions and their expected crystal structures. Based on the aforementioned pattern of the $r_A/r_B$, YHfO, ErHfO, and LuHfO are expected to form the DFP, GdHfO is on the borderline between DFP and OPP, whereas LaHfO and PrHfO are expected to be stabilized in the OPP.[5]

The XRD profiles of the REHfO samples synthesized by direct calcination of the single-source complex precipitates at 650 °C, 1000 °C, and 1500 °C are presented in Figure 3. After direct calcination at 650 °C, amorphous LaHfO and PrHfO were obtained (Figures 3a and 3b). At calcination temperatures of 1000 and 1500 °C, the appearance of weak superstructure peaks (331) and (511) including main diffraction peaks corresponding to the (222), (400), (440), and (622) reflections can be recognized clearly for LaHfO and PrHfO (Figures 3a and 3b), indicating the formation of the pyrochlore phase at this temperature. Contrary to this, poorly crystallized particles were seen for REHfO (RE = Y, Gd, Er, and Lu) samples (Figures 3c–f). Peaks corresponding to the (111), (200), (220), and (311) reflections can be recognized for Y, Gd, Er, and Lu hafnates with the fluorite structure with space group $Fm\bar{3}m$ (JCPDF Card No. 01-80-0471). However, the pyrochlore superstructure reflections, i.e., the main (111) and (311) peaks, were absent in the XRD spectra of LaHfO and PrHfO (JCPDF Card No. 01-078-1617, space group $Fd\bar{3}m$). Samples prepared by direct calcination at 1000 and 1500 °C for 6 h resulted in fully crystalline single phase materials for Y, Gd, Er, and Lu hafnates with all major diffraction peaks identified as the fluorite structure with sharper peaks than corresponding samples prepared at 650 °C. This indicates that these four REHfO (RE = Y, Gd, Er, and Lu) compositions maintained the same fluorite phase even after calcination at 1500 °C for 6 h, although peaks become sharper and more defined with increasing calcination temperature.

We also synthesized these six hafnate REHfO samples (RE = Y, La, Pr, Gd, Er, and Lu) using the MSS method to study how the MSS method would stabilize these compounds compared to the direct calcination method. The MSS synthesis temperature (650 °C) was above the eutectic temperature (230–320 °C) of the added $KNO_3/NaNO_3$ salts and below their decomposition temperatures (~700 °C) to serve as the molten media.[47] Figure 4 shows XRD patterns of the Y, La, Pr,

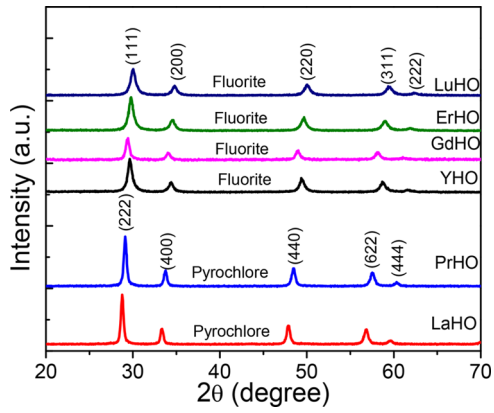


**Figure 4.** XRD patterns of the $RE_2Hf_2O_7$ (Y, La, Pr, Gd, Er, and Lu) samples prepared by the MSS method from the single-source complex precursors at 650 °C for 6 h.

Gd, Er, and Lu hafnate samples synthesized by the MSS route from the single-source complex precursors at 650 °C for 6 h. The intense and sharp diffraction peaks suggest well-crystallized samples. They correspond to disordered fluorite (111), (200), (220), (331), and (221) and ordered pyrochlore (222), (400), (440), (662), and (442) structures with space group $Fm\bar{3}m$ (JCPDF card No. 01-80-0471) and $Fd\bar{3}m$ (ICDD No. 37-1040), respectively. Distinctly, the MSS method endowed highly crystalline LaHfO and PrHfO samples while the direct calcination route only generated amorphous corresponding powders (Figure 3a and 3b) after processing at the same temperature for the same period of time, i.e. both at 650 °C for 6 h. For completeness and comparison, we also attempted to synthesize LaHfO and PrHfO samples using the MSS method under the same conditions at 550 °C. However, no sign of the


DOI: 10.1021/acs.inorgchem.8b02728
Inorg. Chem. 2019, 58, 1241–1251

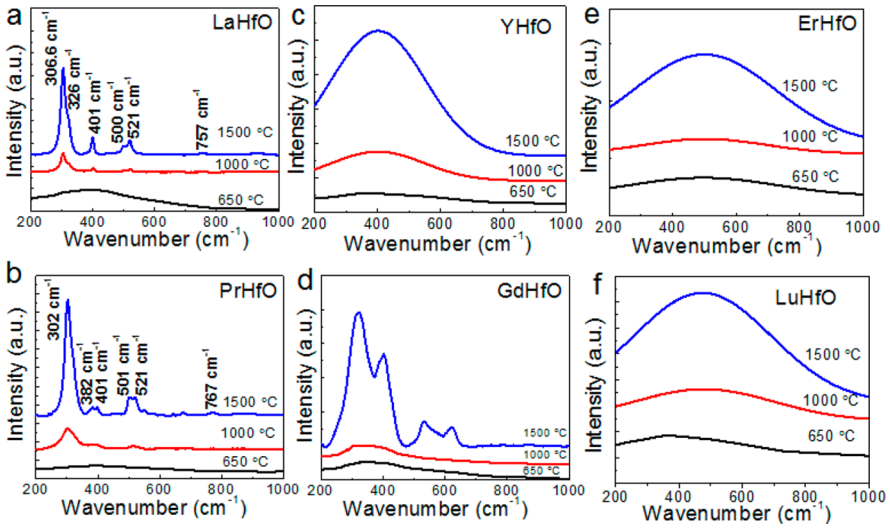


**Figure 5.** Raman spectra of the $RE_2Hf_2O_7$ (RE = Y, La, Pr, Gd, Er, and Lu) samples prepared by direct calcination of the single-source complex precursors at 650 °C, 1000 °C, and 1500 °C in air for 6 h.

formation of crystalline LaHfO and PrHfO was observed based on XRD and Raman data (Figure S3). Therefore, we used 650 °C during our MSS synthesis for the pyrochlore formation in this study.

**3.3. Raman Spectroscopy.** Fluorite and pyrochlore structures have the same parent pattern. The emergence of minor reflections is the only indication of the pyrochlore structure, making accurate quantification by XRD analysis challenging. As reported previously, the absence of pyrochlore phase based on the XRD analysis could be due to its sensitivity to cation sublattice and low XRD resolution with common lab diffractometers.[48] Raman spectroscopy is highly sensitive to metal−oxygen vibrational modes; therefore, it has been used to identify the ordered pyrochlore and disordered fluorite structures of our samples (Figure 5).[49] In the Raman spectra of REHfO, the RE and Hf cations do not contribute to the vibrations since they are located on the inversion center and only vibrations of the oxide ligands are evident.[5] Based on group theory analysis, there are six Raman active modes ($A_{1g}$ + $E_g$ + $4F_{2g}$) for the pyrochlore structure and only one Raman mode ($F_{2g}$) for the fluorite structure within the range of 200 to 1000 $cm^{-1}$.[50] The Raman spectra of our LaHfO and PrHfO samples obtained from direct calcination at 650 °C for 6 h were broad between the 200 and 1000 $cm^{-1}$ region, indicating that these two samples are either in the amorphous phase or in a fluorite phase, which is in agreement with XRD results. After calcination at 1000 °C, several broad Raman peaks appear from the LaHfO and PrHfO compositions indicating their transformation from DFP to OPP (Figure 5a and 5b). While XRD analysis did not demonstrate pyrochlore superstructure reflections of (111) and (311), all the six major Raman modes corresponding to the ordered pyrochlore LaHfO and PrHfO structure were evident after direct calcination, especially at 1500 °C. These peaks corresponded to the $A_{1g}$ mode at 757 and 767 $cm^{-1}$, the $E_g$ mode at 306.6 and 302 $cm^{-1}$, and the $F_{2g}$ bands at ~326, 382, 401, 501, and 521 $cm^{-1}$ (Figures 5a and 5b). The $A_{1g}$ mode is usually assigned to $HfO_6$ octahedra bending vibrations while the $E_g$ mode to O−RE−O bending vibrations.[51] The $F_{2g}$ modes represent a mixture of A−O and B−O bond stretching with bending vibrations. Additional peaks were observed for PrHfO; however, they were not distinct and may be due to scattering from the powder sample. Although the XRD patterns of the directly calcinated LaHfO and PrHfO samples at 1000 and 1500 °C (Figure 3) did not exhibit all the pyrochlore superstructure reflections, the Raman data unambiguously confirms that they have crystallized as pyrochlore structure.

Raman spectra of the Y, Gd, Er, and Lu hafnates consist of broad bands indicating that oxygen ions in the disordered fluorite structure are randomly distributed over the eight anion sites. In comparison with the Raman spectra of the LaHfO and PrHfO samples having ordered pyrochlore structure, we can conclude that the Y, Gd, Er, and Lu hafnates (Figure 5c, 5d, 5e, and 5f), including all those direct calcinated at 650 °C, 1000 °C, and 1500 °C in air for 6 h, possess disordered fluorite structure consistent with group theory. The one exception is GdHfO when calcinated at 1500 °C, where it is thermodynamically transformed into an ordered pyrochlore phase (Figure 5d) due to its borderline radius ratio, as discussed previously by Pokhrel et al.[48] Therefore, based on group theory and the radius ratio rule, LaHfO and PrHfO should stabilize in OPP, but they are only obtained at synthesis temperature ≥1000 °C using the direct calcination route.

Raman spectroscopy was used to further investigate the structure of the samples prepared by the MSS method. All five Raman peaks corresponding to the pyrochlore-type structure of LaHfO and PrHfO were evident (Figure 6) except the peak corresponding to the $HfO_6$ octahedral bending vibration, which usually appears in between 700 $cm^{-1}$ and 800 $cm^{-1}$. Otherwise, Raman modes of the LaHfO and PrHfO samples prepared by the MSS method at 650 °C were almost identical to those synthesized by the direct calcination method at >1000 °C. The absence of peaks corresponding to $HfO_6$ octahedral bending vibrations at or above 700 $cm^{-1}$ indicates that these samples obtained through the MSS method appear to be pure and highly ordered compared to those prepared with direct calcination. In addition, Raman spectra of the Y, Gd, Er, and Lu hafnates prepared by the MSS method at 650 °C are consistent with disordered fluorite structures (Figure S4), similar to those obtained by direct calcination (Figure 5). These Raman results concur with XRD analysis, which shows the formation of the pyrochlore-type structure for the LaHfO


DOI: 10.1021/acs.inorgchem.8b02728
Inorg. Chem. 2019, 58, 1241−1251

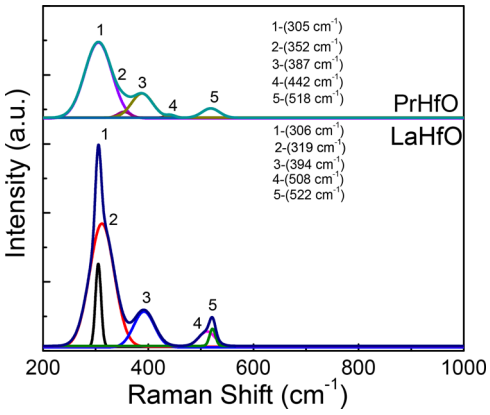


**Figure 6.** Raman spectra of the $RE_2Hf_2O_7$ (RE = La and Pr) samples prepared by the MSS method from the single-source complex precursors at 650 °C for 6 h.

and PrHfO samples by the MSS method at 650 °C. These samples obtained through the MSS method appear to be pure and highly ordered based on our XRD and Raman observations (Figure 4 and 6), which are also consistent with reported XRD and Raman spectra of bulk $La_2Zr_2O_7$.[29]

**3.4. Scanning Electron Microscopy.** The extent of grain size growth as a function of calcination temperature was observed by scanning electron microscopy (SEM) for the as-synthesized powder samples directly calcinated at 650 °C (Figure 7a), 1000 °C (Figure 7b), and 1500 °C (Figure 7c). In general, the grain size increases with increasing calcination temperature. The grain size of the REHfO samples is ∼50−150 nm after direct calcination of the corresponding single-source complex precursors at 650 °C for 6 h (Figure 7a), ∼1.0−1.8 $\mu$m after calcination at 1000 °C (Figure 7b), and ∼1.8−2.8 $\mu$m after calcination to 1500 °C for 6 h (Figure 7c). It is generally believed that grain growth accelerates through Oswald ripening as calcination temperature increases.[52]

Moreover, it was observed from the SEM images that the obtained powders are composed of monodispersed and spherical NPs with well-defined grains after direct calcination of the precursors at 650 °C. However, microplates with flake-like morphology were yielded by calcinating the precursors at higher temperatures. These results demonstrate that direct exposure of the precursors to temperatures ≥1000 °C produces microparticles. Therefore, the efficacy of synthesizing $A_2B_2O_7$ pyrochlore NPs is lost through direct calcination at high temperature. The large pyrochlore microparticle with a low specific surface area will have limited applications in various fields such as catalysis,[53] sensors,[8] energy storage,[54] etc. In summary, while directly calcinating the La and Pr precursors at ≥1000 °C can lead to OPP, their utility is limited by their micron-domain size.

The grain size of the REHfO (Y, La, Pr, Gd, Er, and Lu) samples synthesized by the MSS method at 650 °C for 6 h is ∼20 nm as estimated from the SEM (Figures 8 and S5 to S10) and transmission electron microscopy (TEM) images (Figure S11), which is consistent with the calculated particle size (21.8 ± 0.3 nm) using the Scherrer equation (Table S1). The size distribution of the REHfO complex metal oxide NPs synthesized by the MSS method is extremely narrow with minimum agglomeration due to the presence of the molten salt during the synthesis to separate the formed particles. At a synthesis temperature of 650 °C, the salts were not decomposed to assist the formation of nanostructured REHfO particles with a narrow size distribution, as shown by the SEM/TEM images (Figures 8 and S5 to S11). The small size and narrow distribution of these NPs made by the MSS method are not achievable through conventional solid state and wet chemical reaction methods. For example, Gu et al.[55,56] synthesized micron-sized pyrochlore $La_2Hf_2O_7$ powder at 550 °C using a combustion method, which would not have the efficacy of our NPs as thermally and chemically resistant support for catalysts and chemosensors.[8]

**3.5. Discussion: Superiority of MSS over DC.** The influence of the direct calcination and molten-salt synthesis of the REHfO NPs (RE = Y, La, Pr, Gd, Er, and Lu) samples on their crystal phase (amorphous, fluorite, or pyrochlore) is further summarized in Figure 9 based on $RE^{3+}$ radius, $RE^{3+}$/$Hf^{4+}$ radius ratios, and processing temperature. The crystallization temperature is lower for heavier LuHfO compared to that of lighter LaHfO as represented by line 1 in Figure 9.[5] It should be noted that the direct calcination of the single-source complex precursors $RE(OH)_3{\cdot}HfO(OH)_2{\cdot}nH_2O$ (RE = La, Pr) at 650 °C leads to the formation of amorphous LaHfO and PrHfO only. It is anticipated that homogeneous mixing and fast diffusion of $La(OH)_3$/$Pr(OH)_3$ and $HfO(OH)_2$ components were not achieved at the atomic level in the direct calcination process. Consequently, $La(OH)_3$/$Pr(OH)_3$ and $HfO(OH)_2$ did not react to form pure phase LaHfO and PrHfO samples at the relatively low temperature of 650 °C by direct calcination. The initial single-source precursor forms pyrochlore LaHfO and PrHfO when the calcination temperature increased to 1000 °C or higher as shown by the lines 2, 3, and 4 in Figure 9. Oppositely, the MSS method leads to the formation of stable pyrochlore structures of LaHfO and PrHfO NPs at 650 °C as represented by line 5 in Figure 9. Based on the relevant formation mechanisms of the single-source complex precursors discussed previously (Section 3.1), even though $La(OH)_3$/$Pr(OH)_3$ and $HfO(OH)_2$ may not have mixed homogeneously in the coprecipitated precursors, the liquid mobile molten salt medium can enhance the diffusion of the reactive constituents during the MSS reaction to form the REHfO NPs.[57,58] Once the molten salt is oversaturated with LaHfO and PrHfO, crystals start to precipitate from the molten salt.[57] The precipitation of LaHfO and PrHfO from the oversaturated molten salt leads to further dissolution and reaction of $La(OH)_3$/$Pr(OH)_3$ and $HfO(OH)_2$, which accordingly leads to the formation of more LaHfO and PrHfO nanoparticles.[57] These processes are continually repeated until all of $La(OH)_3$/$Pr(OH)_3$ and $HfO(OH)_2$ reactants have been completely consumed and phase pure LaHfO and PrHfO NPs are obtained. Therefore, in the MSS process, $La(OH)_3$/$Pr(OH)_3$ and $HfO(OH)_2$ rapidly react with each other to form LaHfO and PrHfO NPs.

In the case of Y, Gd, Er, and Lu, it is the hydrated single-source complex precursor $RE(OH)_3{\cdot}HfO(OH)_2{\cdot}nH_2O$ which forms REHfO under thermal decomposition. Therefore, the same mechanism could have helped to form phase pure Y, Gd, Er, and Lu hafnates. More importantly, the MSS synthesis temperature (650 °C) is much lower than that of the direct calcination method (≥1000 °C), which is one major advantage of the MSS method in the preparation of these complex metal oxide NPs from the single-source complex precursors mixed uniformly at the submolecular level. In addition, the MSS method provides a simple pathway for the preparation of ultrasmall and homogeneous NPs without the need for an


DOI: 10.1021/acs.inorgchem.8b02728
Inorg. Chem. 2019, 58, 1241−1251

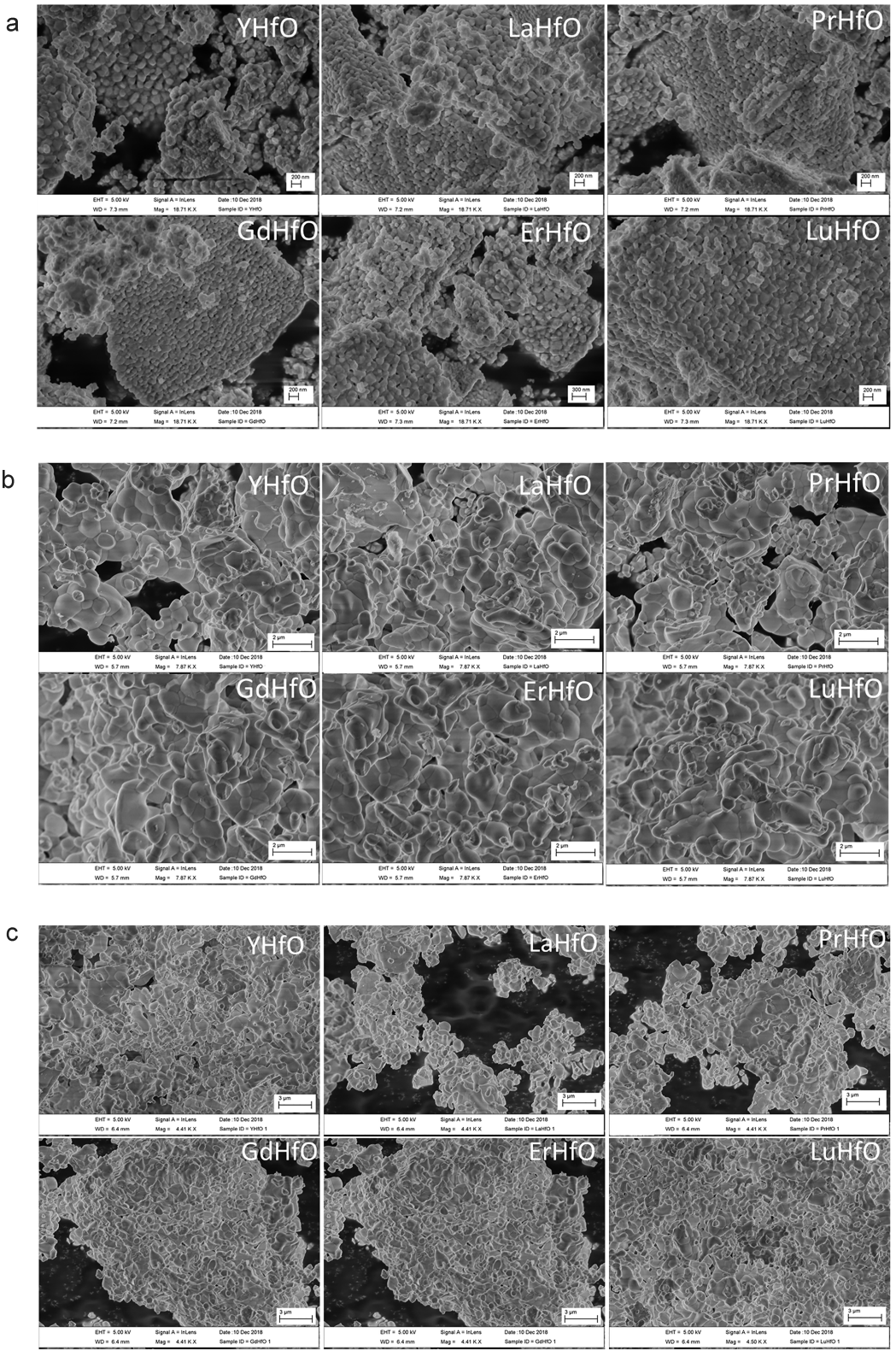


**Figure 7.** SEM images of the REHfO samples (RE = Y, La, Pr, Gd, Er, and Lu) synthesized through direct calcination of the single-source complex precursors at (a) 650 °C, (b) 1000 °C, and (c) 1500 °C in air for 6 h.

organic solvent in chemical synthesis or milling of reactant powders, making this route attractive for scaling-up.

These findings demonstrate the clear advantage of the MSS method when compared to the the direct calcination method. They also indicate that the solubility and diffusion of the La and Pr hydroxide precursors increased in the molten salt medium. Molten salt is believed to enhance the rate of reaction mainly by (1) increasing the contact area of the reactant particles and (2) increasing the mobility of the reactant species.[59] MSS increases the reaction rate, and the product is



DOI: 10.1021/acs.inorgchem.8b02728
*Inorg. Chem.* 2019, 58, 1241−1251

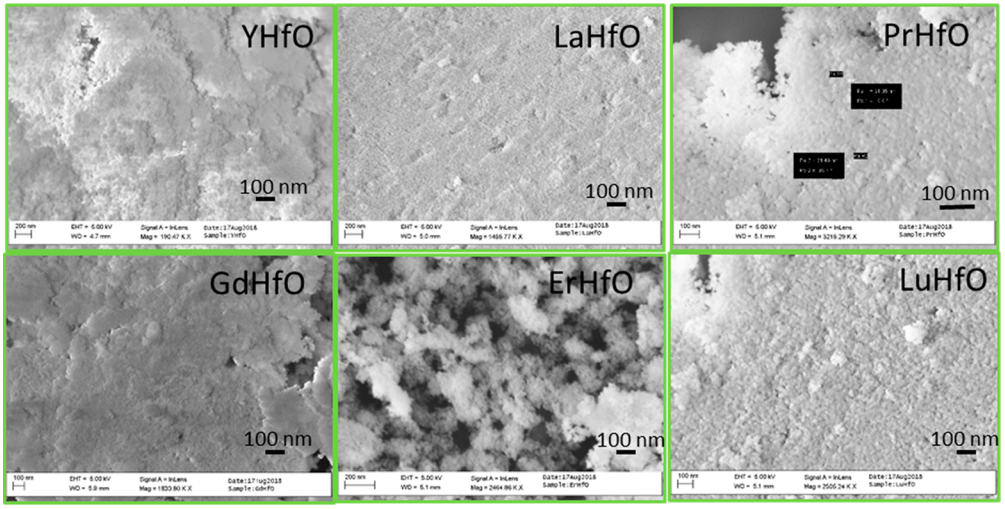


**Figure 8.** SEM images of the $RE_2Hf_2O_7$ (RE = Y, La, Pr, Gd, Er, and Lu) NPs synthesized from the single-source complex precursors through the MSS method at 650 °C for 6 h.

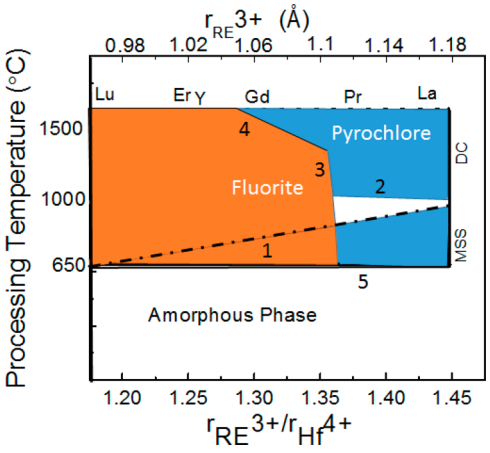


**Figure 9.** Structural evolution scheme of the REHfO (RE = Y, La, Pr, Gd, Er, and Lu) samples from the coprecipitated single-source complex precursors obtained by the DC and MSS methods based on $RE^{3+}$ radius, $RE^{3+}/Hf^{4+}$ radius ratio, and calcination temperature. Line 1: crystallization temperature based on DSC from ref 5. Lines 2, 3, and 4: pyrochlore phase transition temperature obtained after direct calcination of the $RE(OH)_3{\cdot}HfO(OH)_2{\cdot}nH_2O$ (RE = La, Gd, and Pr) to obtain LaHfO and GdHfO and PrHfO (transition temperature), and line 5: molten-salt synthesis temperature (650 °C).

formed at a lower temperature in two stages, which are the (a) reaction and (b) particle-growth stages.[60] In the reaction stage, the particles are formed in the presence of reactant. The reactants dissolve in the molten salt and product particles form. In this situation, the dissolution/precipitation process is expected to be dominant, which favors the crystal growth.[61] This MSS reaction system consists of solid product particles and molten salt. Ostwald ripening governs the growth of the particles. The particles that are smaller than critical size are then dissolved in the molten salt medium.[62] Moreover, the GdHfO compound made by the direct calcination route goes through a phase transformation from fluorite to pyrochlore when the calcination temperature increases (line 4 in Figure 9). The pyrochlore ordering for borderline compound GdHfO was confirmed based on Raman analysis (Figure 5).

## 4. CONCLUSION

Synthesis of $RE_2Hf_2O_7$ hafnates (RE = Y, La, Pr, Gd, Er, and Lu) by direct calcination or molten salt synthesis process of coprecipitated single-source complex precursors has been investigated using characterization methods including XRD, Raman spectroscopy, and SEM. We have demonstrated the clear advantages of the low-temperature MSS method for REHfO (RE = La and Pr) pyrochlore NPs over the direct calcination method. The structural analysis highlights that the MSS method can produce stable pyrochlore LaHfO and PrHfO NPs at temperatures as low as 650 °C, while the direct calcination method must reach temperature ≥1000 °C to yield phase pure samples. Moreover, the MSS method allows for the synthesis of NPs with narrow size distribution, while the direct calcination method produces coarse micron-sized particles, severely diminishing many potential applications of these materials. MSS is, therefore, an ideal method of fabricating pyrochlore NPs at a relatively low synthesis temperature.

## ■ ASSOCIATED CONTENT

### Supporting Information

The Supporting Information is available free of charge on the ACS Publications website at DOI: 10.1021/acs.inorgchem.8b02728.

Raman spectra, SEM images with histogram included for particle size evaluation of the REHfO NPs (RE = Y, La, Pr, Gd, Er, and Lu) synthesized through the MSS method, TEM images of the LaHfO and PrHfO, and Scherrer calculations of their particle sizes (PDF)

## ■ AUTHOR INFORMATION

### Corresponding Author

*Tel: +1 956 665 2986; Fax: +1 956 665 5006; E-mail: yuanbing.mao@utrgv.edu.

### ORCID

Santosh K. Gupta: 0000-0002-1178-0159

Yuanbing Mao: 0000-0003-2665-6676

### Notes

The authors declare no competing financial interest.



DOI: 10.1021/acs.inorgchem.8b02728
Inorg. Chem. 2019, 58, 1241−1251

## ■ ACKNOWLEDGMENTS

The authors thank the Defense Threat Reduction Agency (DTRA) of the U.S. Department of Defense (award #HDTRA1-10-1-0114), USDA National Institute of Food and Agriculture (award number: 2015-38422-24059), and the National Science Foundation under CHE (award #1710160) and DMR grant #1523577. The authors also thank James Hinthorne and Julio Cantu with assistance in XRD measurements and high temperature calcination, respectively. KW thanks the UTRGV Science Education Grant #52007568 funded by the Howard Hughes Medical Institute. SKG thanks the United States–India Education Foundation (USIEF) and Institute of International Education (IIE) for his Fulbright Nehru Postdoctoral Fellowship (Award# 2268/FNPDR/2017).

## ■ REFERENCES

(1) Ramirez, A. P.; Hayashi, A.; Cava, R. a.; Siddharthan, R.; Shastry, B. Zero-point entropy in 'spin ice'. *Nature* **1999**, *399*, 333.
(2) Gardner, J. S.; Gingras, M. J.; Greedan, J. E. Magnetic pyrochlore oxides. *Rev. Mod. Phys.* **2010**, *82*, 53.
(3) Levi, C. G. Emerging materials and processes for thermal barrier systems. *Curr. Opin. Solid State Mater. Sci.* **2004**, *8*, 77–91.
(4) Sickafus, K. E.; Minervini, L.; Grimes, R. W.; Valdez, J. A.; Ishimaru, M.; Li, F.; McClellan, K. J.; Hartmann, T. Radiation tolerance of complex oxides. *Science* **2000**, *289*, 748–751.
(5) Popov, V.; Menushenkov, A.; Yaroslavtsev, A.; Zubavichus, Y. V.; Gaynanov, B.; Yastrebtsev, A.; Leshchev, D.; Chernikov, R. Fluorite-pyrochlore phase transition in nanostructured $Ln_2Hf_2O_7$ (Ln= La-Lu). *J. Alloys Compd.* **2016**, *689*, 669–679.
(6) Shu, X.; Fan, L.; Xie, Y.; Zhu, W.; Pan, S.; Ding, Y.; Chi, F.; Wu, Y.; Lu, X. Alpha-particle irradiation effects on uranium-bearing $Gd_2Zr_2O_7$ ceramics for nuclear waste forms. *J. Eur. Ceram. Soc.* **2017**, *37*, 779–785.
(7) Lian, J.; Wang, L.; Wang, S.; Chen, J.; Boatner, L.; Ewing, R. Nanoscale manipulation of pyrochlore: new nanocomposite ionic conductors. *Phys. Rev. Lett.* **2001**, *87*, 145901.
(8) Sevast'yanov, V. G.; Simonenko, E. P.; Simonenko, N. P.; Sakharov, K. A.; Kuznetsov, N. T. Synthesis of finely dispersed $La_2Zr_2O_7$, $La_2Hf_2O_7$, $Gd_2Zr_2O_7$ and $Gd_2Hf_2O_7$ oxides. *Mendeleev Commun.* **2013**, *1*, 17–18.
(9) Zhou, G.; Wang, Z.; Zhou, B.; Zhao, Y.; Zhang, G.; Wang, S. Fabrication of transparent $Y_2Hf_2O_7$ ceramics via vacuum sintering. *Opt. Mater.* **2013**, *35*, 774–777.
(10) An, L.; Ito, A.; Goto, T. Fabrication of transparent lutetium oxide by spark plasma sintering. *J. Am. Ceram. Soc.* **2011**, *94*, 695–698.
(11) Wahid, K.; Pokhrel, M.; Mao, Y. Structural, photoluminescence and radioluminescence properties of $Eu^{3+}$ doped $La_2Hf_2O_7$ nanoparticles. *J. Solid State Chem.* **2017**, *245*, 89–97.
(12) Durand, A. M.; Klavins, P.; Corruccini, L. Heat capacity of the frustrated magnetic pyrochlores $Gd_2Zr_2O_7$ and $Gd_2Hf_2O_7$. *J. Phys.: Condens. Matter* **2008**, *20*, 235208.
(13) Anand, V.; Opherden, L.; Xu, J.; Adroja, D.; Islam, A.; Herrmannsdörfer, T.; Hornung, J.; Schönemann, R.; Uhlarz, M.; Walker, H. Physical properties of the candidate quantum spin-ice system $Pr_2Hf_2O_7$. *Phys. Rev. B: Condens. Matter Mater. Phys.* **2016**, *94*, 144415.
(14) Cepeda-Sánchez, N. M.; Díaz-Guillén, J. A.; Maczka, M.; Amador, U.; Fuentes, A. F. Mechanochemical synthesis, crystal structure and ion conduction in the $Gd_2Hf_{2-x}Ti_xO_7$ system. *J. Mater. Sci.* **2017**, *52*, 11933–11946.
(15) Gupta, S. K.; Mohapatra, M.; Natarajan, V.; Godbole, S. Site-specific luminescence of $Eu^{3+}$ in gel-combustion-derived strontium zirconate perovskite nanophosphors. *J. Mater. Sci.* **2012**, *47*, 3504–3515.
(16) Zhang, Y.-W.; Si, R.; Liao, C.-S.; Yan, C.-H.; Xiao, C.-X.; Kou, Y. Facile alcohothermal synthesis, size-dependent ultraviolet absorption, and enhanced CO conversion activity of ceria nanocrystals. *J. Phys. Chem. B* **2003**, *107*, 10159–10167.
(17) Tang, Z.; Huang, Z.; Qi, J.; Guo, X.; Han, W.; Zhou, M.; Peng, S.; Lu, T. Synthesis and characterization of $Gd_2Zr_2O_7$ defect-fluorite oxide nanoparticles via a homogeneous precipitation-solvothermal method. *RSC Adv.* **2017**, *7*, 54980–54985.
(18) Rahimi-Nasrabadi, M.; Mahdavi, S.; Adib, K. Controlled synthesis and characterization of $Dy_2Ti_2O_7$ nanoparticles through a facile approach. *J. Mater. Sci.: Mater. Electron.* **2017**, *28*, 16133–16140.
(19) Chen, H.; Gao, Y.; Liu, Y.; Luo, H. Coprecipitation synthesis and thermal conductivity of $La_2Zr_2O_7$. *J. Alloys Compd.* **2009**, *480*, 843–848.
(20) Wang, Q.; Cheng, X.; Li, J.; Jin, H. Hydrothermal synthesis and photocatalytic properties of pyrochlore $Sm_2Zr_2O_7$ nanoparticles. *J. Photochem. Photobiol., A* **2016**, *321*, 48–54.
(21) Mani, R.; Jiang, H.; Gupta, S. K.; Li, Z.; Duan, X. Role of synthesis method on luminescence properties of europium (II, III) ions in $\beta$-$Ca_2SiO_4$: probing local site and structure. *Inorg. Chem.* **2018**, *57*, 935–950.
(22) Gupta, S. K.; Sudarshan, K.; Ghosh, P.; Srivastava, A.; Bevara, S.; Pujari, P.; Kadam, R. Role of various defects in the photoluminescence characteristics of nanocrystalline $Nd_2Zr_2O_7$: an investigation through spectroscopic and DFT calculations. *J. Mater. Chem. C* **2016**, *22*, 4988–5000.
(23) Gupta, S. K.; Ghosh, P. S.; Yadav, A. K.; Pathak, N.; Arya, A.; Jha, S. N.; Bhattacharyya, D.; Kadam, R. M. Luminescence properties of $SrZrO_3/Tb^{3+}$ perovskite: host-dopant energy-transfer dynamics and local structure of $Tb^{3+}$. *Inorg. Chem.* **2016**, *55*, 1728–1740.
(24) Gupta, S. K.; Ghosh, P. S.; Yadav, A. K.; Jha, S. N.; Bhattacharyya, D.; Kadam, R. M. Origin of blue-green emission in $\alpha$-$Zn_2P_2O_7$ and local structure of $Ln^{3+}$ ion in $\alpha$-$Zn_2P_2O_7$: Ln3+ (Ln= Sm, Eu): time-resolved photoluminescence, EXAFS, and DFT measurements. *Inorg. Chem.* **2017**, *56*, 167–178.
(25) Wang, S.; Zhou, G.; Lu, M.; Zhou, Y.; Wang, S.; Yang, Z. Synthesis and characterization of lanthanum stannate nanoparticles. *J. Am. Ceram. Soc.* **2006**, *89*, 2956–2959.
(26) Nair, J.; Nair, P.; Doesburg, E.; Van Ommen, J.; Ross, J.; Burggraaf, A.; Mizukami, F. Preparation and characterization of lanthanum zirconate. *J. Mater. Sci.* **1998**, *33*, 4517–4523.
(27) Huang, Z.; Duan, H.; Liu, J.; Zhang, H. Preparation of lanthanum cerate powders via a simple molten salt route. *Ceram. Int.* **2016**, *42*, 10482–10486.
(28) Matsumura, Y.; Yoshinaka, M.; Hirota, K.; Yamaguchi, O. Formation and sintering of $La_2Zr_2O_7$ by the hydrazine method. *Solid State Commun.* **1997**, *104*, 341–345.
(29) Kong, L.; Karatchevtseva, I.; Gregg, D. J.; Blackford, M. G.; Holmes, R.; Triani, G. A novel chemical route to prepare $La_2Zr_2O_7$ pyrochlore. *J. Am. Ceram. Soc.* **2013**, *96*, 935–941.
(30) Mao, Y.; Guo, X.; Huang, J. Y.; Wang, K. L.; Chang, J. P. Luminescent nanocrystals with $A_2B_2O_7$ composition synthesized by a kinetically modified molten salt method. *J. Phys. Chem. C* **2009**, *113*, 1204–1208.
(31) Pokhrel, M.; Wahid, K.; Mao, Y. Systematic Studies on $RE_2Hf_2O_7$:5%$Eu^{3+}$ (RE = Y, La, Pr, Gd, Er, and Lu) Nanoparticles: Effects of the A-Site $RE^{3+}$ Cation and Calcination on Structure and Photoluminescence. *J. Phys. Chem. C* **2016**, *120*, 14828–14839.
(32) Pokhrel, M.; Brik, M. G.; Mao, Y. Particle size and crystal phase dependent photoluminescence of $La_2Zr_2O_7$:$Eu^{3+}$ nanoparticles. *J. Am. Ceram. Soc.* **2015**, *98*, 3192–3201.
(33) Pokhrel, M.; Burger, A.; Groza, M.; Mao, Y. Enhance the photoluminescence and radioluminescence of $La_2Zr_2O_7$:$Eu^{3+}$ core nanoparticles by coating with a thin $Y_2O_3$ shell. *Opt. Mater.* **2017**, *68*, 35–41.
(34) Li, C.; Yang, J.; Yang, P.; Lian, H.; Lin, J. Hydrothermal synthesis of lanthanide fluorides $LnF_3$ (Ln= La to Lu) nano-/


DOI: 10.1021/acs.inorgchem.8b02728
*Inorg. Chem.* 2019, 58, 1241–1251

microcrystals with multiform structures and morphologies. *Chem. Mater.* **2008**, *20*, 4317−4326.
(35) Wang, X.; Li, Y. Synthesis and characterization of lanthanide hydroxide single-crystal nanowires. *Angew. Chem., Int. Ed.* **2002**, *41*, 4790−4793.
(36) Yan, R.; Sun, X.; Wang, X.; Peng, Q.; Li, Y. Crystal structures, anisotropic growth, and optical properties: controlled synthesis of lanthanide orthophosphate one-dimensional nanomaterials. *Chem. - Eur. J.* **2005**, *11*, 2183−2195.
(37) Meloche, C. C.; Vratny, F. Solubility product relations in the rare earth hydrous hydroxides. *Anal. Chim. Acta* **1959**, *20*, 415−418.
(38) Kalaji, A.; Soderholm, L. A novel nonanuclear hafnium oxide−hydroxide−sulphate cluster crystallised from aqueous solution. *Chem. Commun.* **2014**, *50*, 997−999.
(39) Geng, F.; Matsushita, Y.; Ma, R.; Xin, H.; Tanaka, M.; Iyi, N.; Sasaki, T. Synthesis and properties of well-crystallized layered rare-earth hydroxide nitrates from homogeneous precipitation. *Inorg. Chem.* **2009**, *48*, 6724−6730.
(40) Jia, G.; Liu, K.; Zheng, Y.; Song, Y.; Yang, M.; You, H. Highly uniform $Gd(OH)_3$ and $Gd_2O_3{:}Eu^{3+}$ nanotubes: facile synthesis and luminescence properties. *J. Phys. Chem. C* **2009**, *113*, 6050−6055.
(41) Abbasi, A.; Lindqvist-Reis, P.; Eriksson, L.; Sandström, D.; Lidin, S.; Persson, I.; Sandström, M. Highly hydrated cations: deficiency, mobility, and coordination of water in crystalline nonahydrated scandium (III), yttrium (III), and lanthanoid (III) trifluoromethanesulfonates. *Chem. - Eur. J.* **2005**, *11*, 4065−4077.
(42) Haschke, J. M. Preparation, phase equilibriums, crystal chemistry, and some properties of lanthanide hydroxide nitrates. *Inorg. Chem.* **1974**, *13*, 1812−1818.
(43) Shannon, R. Revised effective ionic radii and systematic studies of interatomic distances in halides and chalcogenides. *Acta Crystallogr., Sect. A: Cryst. Phys., Diffr., Theor. Gen. Crystallogr.* **1976**, *32*, 751−767.
(44) Fajans, K.; Joos, G. Molrefraktion von ionen und molekülen im lichte der atomstruktur. *Eur. Phys. J. A* **1924**, *23*, 1−46.
(45) Shannon, R. D. Revised effective ionic radii and systematic studies of interatomic distances in halides and chalcogenides. *Acta Crystallogr., Sect. A: Cryst. Phys., Diffr., Theor. Gen. Crystallogr.* **1976**, *32*, 751−767.
(46) Subramanian, M.; Aravamudan, G.; Rao, G. S. Oxide pyrochlores—a review. *Prog. Solid State Chem.* **1983**, *15*, 55−143.
(47) Singh, N. B.; Ojha, A. K. Formation of copper oxide through $NaNO_3$−$KNO_3$ eutectic melt and its catalytic activity in the decomposition of ammonium perchlorate. *Thermochim. Acta* **2002**, *390*, 67−72.
(48) Pokhrel, M.; Wahid, K.; Mao, Y. Systematic studies on $RE_2Hf_2O_7$: 5% $Eu^{3+}$ (RE= Y, La, Pr, Gd, Er, and Lu) nanoparticles: effects of the A-site $RE^{3+}$ cation and calcination on structure and photoluminescence. *J. Phys. Chem. C* **2016**, *120*, 14828−14839.
(49) Sayed, F. N.; Grover, V.; Bhattacharyya, K.; Jain, D.; Arya, A.; Pillai, C. G. S.; Tyagi, A. K. $Sm_{2-x}Dy_xZr_2O_7$ pyrochlores: Probing order−disorder dynamics and multifunctionality. *Inorg. Chem.* **2011**, *50*, 2354−2365.
(50) Gupta, S. K.; Zuniga, J. P.; Ghosh, P. S.; Abdou, M.; Mao, Y. Correlating structure and luminescence properties of undoped and $Eu^{3+}$-doped $La_2Hf_2O_7$ nanoparticles prepared with different coprecipitating pH values through experimental and theoretical studies. *Inorg. Chem.* **2018**, *57*, 11815−11830.
(51) Turner, K. M.; Rittman, D. R.; Heymach, R. A.; Tracy, C. L.; Turner, M. L.; Fuentes, A. F.; Mao, W. L.; Ewing, R. C. Pressure-induced structural modifications of rare-earth hafnate pyrochlore. *J. Phys.: Condens. Matter* **2017**, *29*, 255401.
(52) Voorhees, P. W. The theory of Ostwald ripening. *J. Stat. Phys.* **1985**, *38*, 231−252.
(53) Benčina, M.; Valant, M. $Bi_2Ti_2O_7$-based pyrochlore nanoparticles and their superior photocatalytic activity under visible light. *J. Am. Ceram. Soc.* **2018**, *101*, 82−90.
(54) Lebedev, D.; Povia, M.; Waltar, K.; Abdala, P. M.; Castelli, I. E.; Fabbri, E.; Blanco, M. V.; Fedorov, A.; Copéret, C.; Marzari, N.; Schmidt, T. J. Highly active and stable iridium pyrochlores for oxygen evolution reaction. *Chem. Mater.* **2017**, *29*, 5182−5191.
(55) Gu, S.; Zhang, S.; Xue, B.; Yan, J.; Li, W.; Zhang, L. Phase variation and thermophysical properties of $La_2Hf_2O_7$ with alumina addition. *J. Eur. Ceram. Soc.* **2018**, *38*, 1938−1945.
(56) Gu, S.; Zhang, S.; Xu, D.; Li, W.; Yan, J. Evolution of microstructure and hot corrosion performance of $La_2Hf_2O_7$ ceramic in contact with molten sulfate-vanadate salt. *Ceram. Int.* **2018**, *44*, 2048−2057.
(57) Li, Z.; Lee, W. E.; Zhang, S. Low-Temperature Synthesis of $CaZrO_3$ Powder from Molten Salts. *J. Am. Ceram. Soc.* **2007**, *90*, 364−368.
(58) Li, Z.; Zhang, S.; Lee, W. E. Molten salt synthesis of $LaAlO_3$ powder at low temperatures. *J. Eur. Ceram. Soc.* **2007**, *27*, 3201−3205.
(59) Arendt, R.; Rosolowski, J.; Szymaszek, J. Lead zirconate titanate ceramics from molten salt solvent synthesized powders. *Mater. Res. Bull.* **1979**, *14*, 703−709.
(60) Kimura, T.; Yamaguchi, T. Fused salt synthesis of $Bi_4Ti_3O_{12}$. *Ceram. Int.* **1983**, *9*, 13−17.
(61) Zhao, L.; Gao, F.; Zhang, C.; Zhao, M.; Tian, C. Molten salt synthesis of anisometric $KSr_2Nb_5O_{15}$ particles. *J. Cryst. Growth* **2005**, *276*, 446−452.
(62) Rahaman, M. N. *Ceramic Processing*; CRC Press: 2017.


DOI: 10.1021/acs.inorgchem.8b02728
*Inorg. Chem.* 2019, 58, 1241−1251